



Supplementary Materials for

WS₂ ribbon arrays with defined chirality and coherent polarity

Guodong Xue *et al.*

Corresponding authors: Feng Ding, f.ding@siat.ac.cn; Zhongming Wei, zmwei@semi.ac.cn; Can Liu, canliu@ruc.edu.cn;
Kaihui Liu, khliu@pku.edu.cn

Science **384**, 1100 (2024)
DOI: 10.1126/science.adn9476

The PDF file includes:

Materials and Methods
Figs. S1 to S16

S1 Materials and Methods

S1.1 Annealing of the sapphire substrates

The 2-inch single-side polished α - Al_2O_3 , $\sim 1^\circ$ miscutting c/m and $c/\pm R15^\circ$ Al_2O_3 were specially ordered from Dongda Times (Chengdu) Technology Co., LTD. The annealing process was carried out at 1,100–1,300 $^\circ\text{C}$ in air for 10 hours, in order to form uniform aligned steps on sapphire.

S1.2 Pre-evaporation of the Na_2WO_4 precursors

A piece of fused silica was first pre-treated by O_2 plasma for 5 minutes, followed by the spin-coating or dip-coating process of the Na_2WO_4 aqueous solution with optimized concentrations (typically 1 mg mL^{-1} , 10 mg mL^{-1} , 20 mg mL^{-1} and 30 mg mL^{-1}). After drying in Ar atmosphere, the precursor-coated fused silica and annealed sapphire were placed in a face-to-face manner and then loaded into the hot-wall tube furnace (Tianjin Kaiheng Co. Ltd, custom designed). The furnace was ramped to 850 $^\circ\text{C}$ in 1 hour and maintained at this temperature for 10 minutes with 100 sccm Ar. During the pre-evaporation process, the system pressure was kept at ~ 120 Pa. After cooling down to room temperature, uniform Na_2WO_4 particles were deposited onto the sapphire substrates.

S1.3 Growth of WS_2 ribbon arrays

A piece of ZnS plate was posited upper the pre-deposited sapphire substrate, and then placed together into the central zone of the tube furnace. The chamber of the furnace was flushed with 100 sccm Ar for 5 minutes before ramping to the optimized temperature. The ribbon growth was carried out at 930 $^\circ\text{C}$ for 1-4 hours under a mixed gas flow (100 sccm Ar, 2 sccm H_2). After the growth, the system was naturally cooled down to room temperature.

S1.4 Characterizations of WS_2 ribbons

- (i) *Optical measurements.* Optical images were taken with an Olympus BX51M microscope. Raman measurements were performed using a WITec alpha300R system with a laser excitation wavelength of 514 nm and a power of ~ 1 mW. Second harmonic generation (SHG) measurements were obtained with an excitation wavelength of 1,064 nm and an average power of 800 μW . The polarization-dependent SHG pattern measurements were performed using the same system by adding a half-wave plate in front of the focusing objective in a reflection

geometry. A linear analyzer parallel to the incident polarization was utilized to extract the parallel component of SHG from the sample.

- (ii) *Transmission electron microscopy (TEM) characterizations.* The WS₂ ribbons were transferred onto TEM grids by the polymethylmethacrylate (PMMA) based method. DF-TEM, STEM and SAED experiments were performed in the FEI Titan Themis G2 300 operated at 300 kV, and the size of the selected area aperture during the diffraction experiment was chosen to be ~200 nm.
- (iii) *Atomic force microscopy (AFM), scanning electron microscopy (SEM) and auger electron spectroscopy (AES) measurements.* AFM images were acquired using an Asylum Research Cypher AFM system. SEM measurements were carried out by the FEI Nova NanoSEM 430 scanning electron microscope for summarizing the geometric parameters of ribbons. For AES measurements, 100-nm-thick Au was deposited onto the as-grown WS₂ ribbons and then gently peeled the WS₂/Au stack with the assistance of the optical adhesive (Norland, No. 61). The AES characterizations were carried out using a PHI 710 scanning Auger nanoprobe instrument.

S1.5 Computational details

Geometric optimization and energy calculations of the Na₂WO₄/sapphire and Na₂WO₄/WS₂ systems were carried out using density functional theory (DFT) as implemented in Vienna Ab-initio Simulation Package (VASP). The generalized gradient approximation (GGA) with the Perdew-Burke-Ernzerhof (PBE) exchange-correlation function was used with the plane-wave cutoff energy set at 400 eV for all calculations. The dispersion-corrected DFT-D3 method was used because of its good description of long-range van der Waals interactions for multi-layered two-dimensional materials. The geometries of the structures were relaxed until the force on each atom was less than 0.1 eV Å⁻¹, and the energy convergence criterion of 1×10⁻⁴ eV was met. In the out-of-plane direction, the vacuum spacing between neighboring images was set at least 10 Å to avoid a periodic imaging interaction. The formation energy of Na₂WO₄ clusters bonded Al₂O₃ system with and without steps can be mathematically calculated as $E_F = (E_t - E_{sub} - E_{Na_2WO_4})/N$, where E_t and E_{sub} are the total energies of Na₂WO₄/Al₂O₃ system and the Al₂O₃ substrate with and without steps, respectively. $E_{Na_2WO_4}$ is the energy of Na₂WO₄ clusters. N is the number of atoms in the Na₂WO₄ clusters.

S1.6 Numerical simulation of the SHG signal

The polarization-dependent SHG signal of WS₂ ribbon was numerically simulated using a frequency-domain finite-element solver in COMSOL Multiphysics based on wave optics module. To match the experimental conditions, the excitation light was modelled by a Gaussian beam with a wavelength of 1,064 nm and a spot diameter of 1 μm . The SHG intensity was obtained by integrating the signal in the SHG emission core.

S1.7 BPVE device fabrication

In order to obtain a flat and clean metal-semiconductor interface, the 100-nm-thick Au electrodes fabricated on Si/SiO₂ substrate were directly transferred onto the target ribbons with the assistance of the polypropylene carbonate (PPC) film. Afterwards, the polymer film could be removed by annealing at 280 °C in the furnace chamber with 100 sccm Ar at low-pressure condition. For the process of integrated ribbon devices, the electrodes were fabricated through electron beam lithography (EBL) (for patterning PMMA resists), electron beam evaporation (for depositing metal), and a lift-off process. For the discrete ribbon devices, the second EBL was utilized to pattern PMMA for protecting, and then the reactive ion etching (RIE) process with 30 mW at the atmosphere of O₂/CHF₃ (1:10) was utilized to etch the unprotected ribbons.

S1.8 Photovoltaic response measurements

The electrical measurements of *I-V* characterizations and polarized photocurrent were carried out by a semiconductor device analyzer (Agilent-B1500) under ambient conditions. Ribbons were illuminated by the LDPSSL-laser (wavelength of 450 nm) with a spot size of $\sim 1 \mu\text{m}$. For the linear polarized laser, the composite lens of the Glan-Taylor prism and the half-wave plate were located before the 50 \times objective lens. The photocurrent mapping was carried out by the MStarter 200 scanning system.

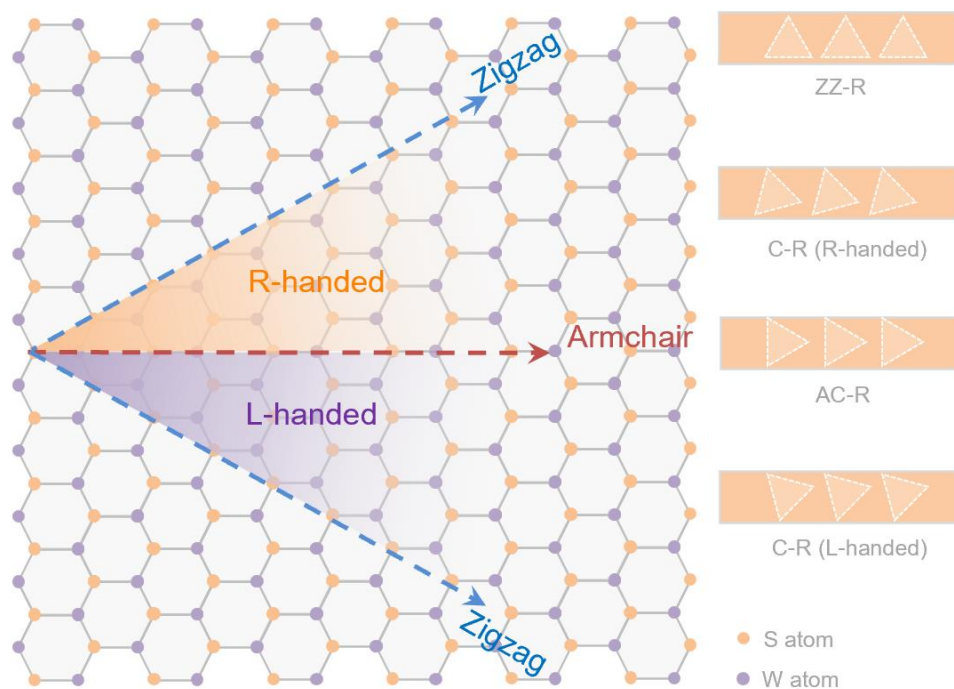


Fig. S1. Axial chirality definition of WS₂ ribbons. The axis of zigzag (ZZ-R) and armchair ribbon (AC-R) are aligned along the zigzag (blue dashed line) and armchair (red dashed line) lattice chains, respectively. Chiral ribbons (C-R) are classified into left-handed (L-handed) and right-handed (R-handed) species within ribbon axis located at the purple and orange regions, respectively. The dashed triangles marked in right panel indicate the relationship between WS₂ crystalline direction and ribbon axis orientation.

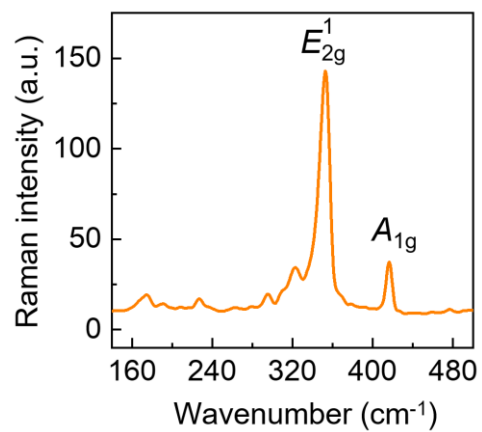


Fig. S2. Typical Raman spectrum of the as-grown WS₂ ribbons.

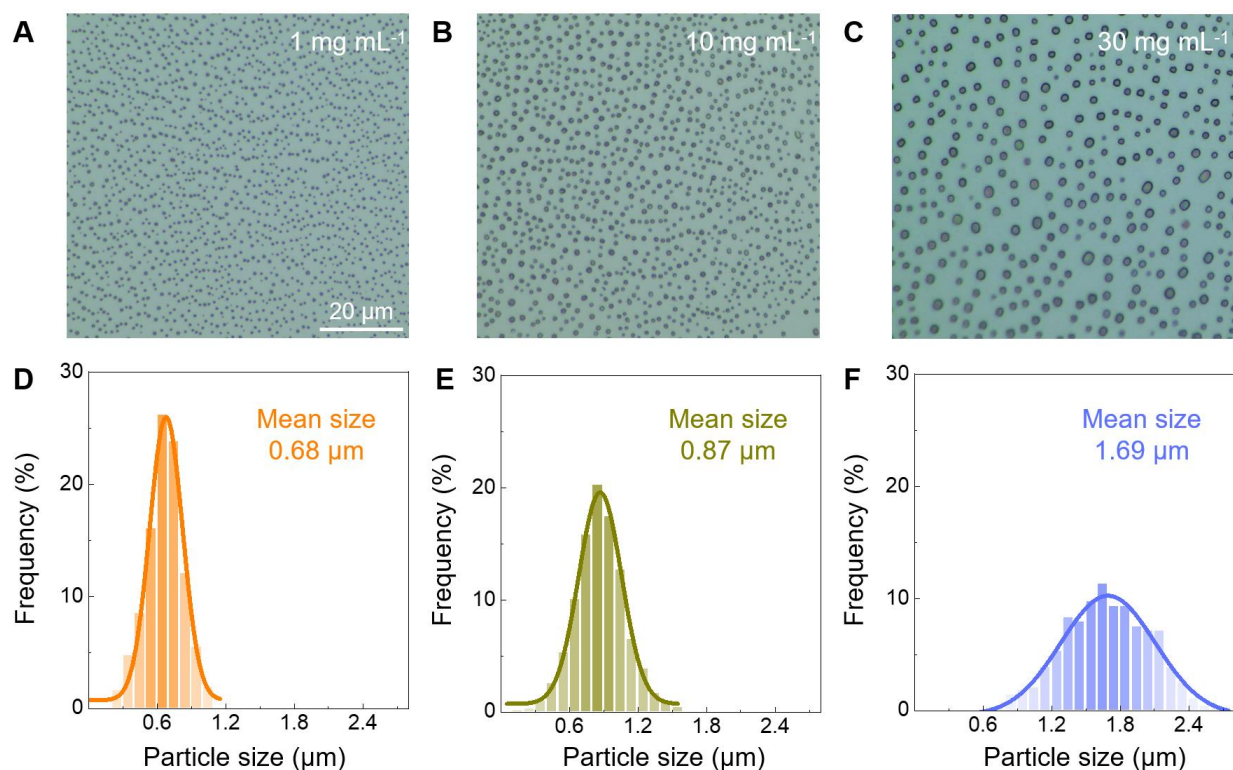


Fig. S3. Size controllability of the pre-evaporated Na_2WO_4 particles. (A-C) Optical images of the Na_2WO_4 particles at spin-coated aqueous solution concentration of 1 mg mL^{-1} (A), 10 mg mL^{-1} (B) and 30 mg mL^{-1} (C), respectively. (D-F) Statistical distributions of Na_2WO_4 particle sizes analyzed from the images in (A-C).

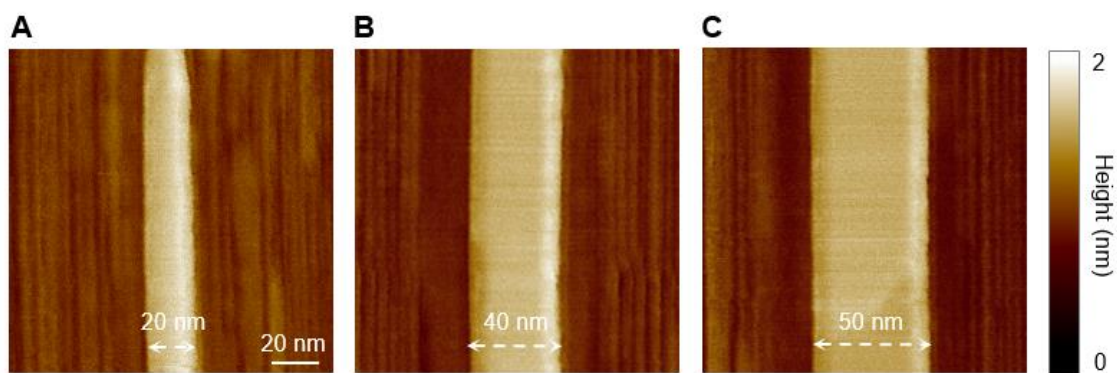


Fig. S4. The as-grown WS₂ ribbons with widths under 100 nm. (A-C) AFM images of WS₂ ribbons with typical widths of around 20 nm (A), 40 nm (B) and 50 nm (C), respectively. All images are of the same size.

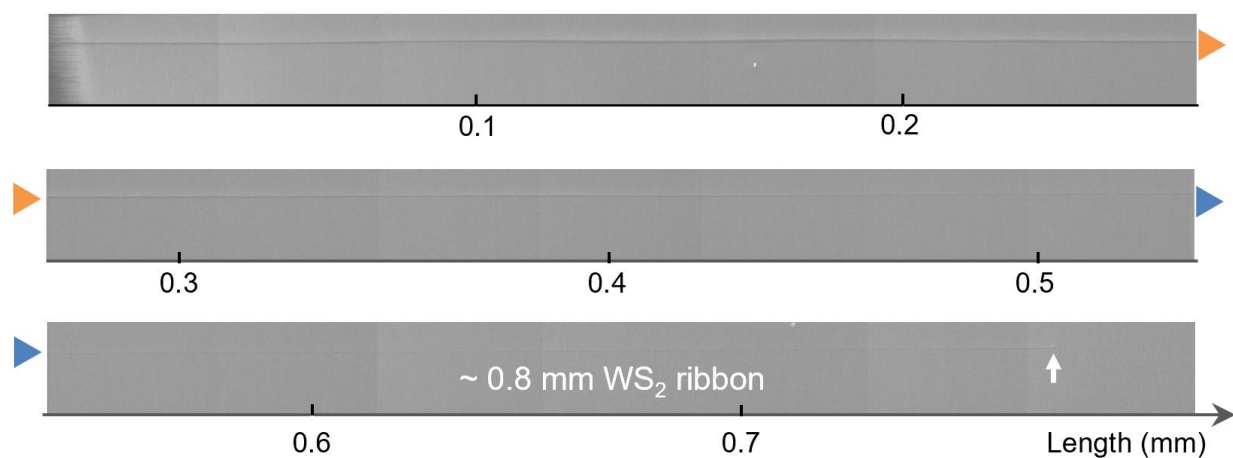


Fig. S5. SEM images of an ultralong WS₂ ribbon obtained by extending the growth duration to 4 hours. The marker pairs in orange and blue represent stitching points of the ribbon between different SEM images. The total length of the ribbon is around 0.8 mm.

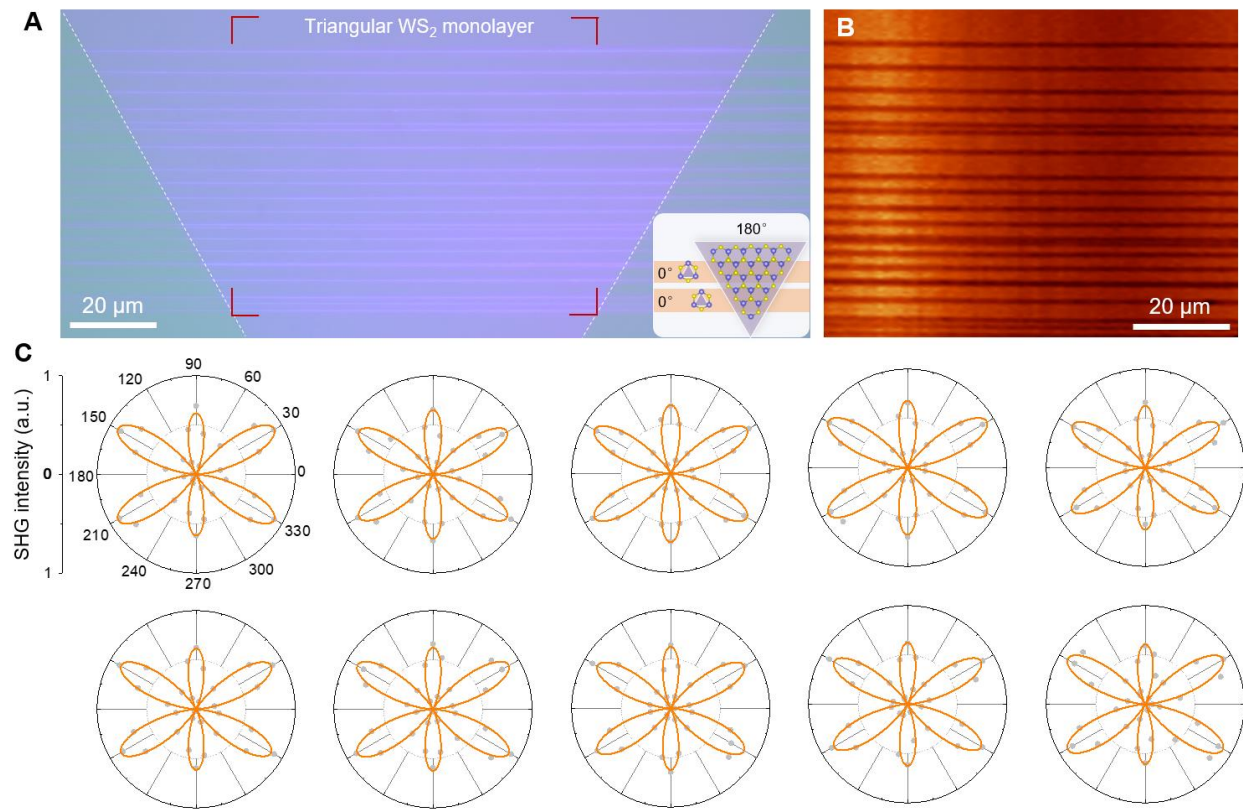


Fig. S6. Characterization of the polarity and chirality of a large-scale WS₂ ribbon array. (A) Optical image of a large-scale zigzag WS₂ ribbon array covered by a transferred triangular WS₂ monolayer. (B) SHG mapping of the ribbons/WS₂ stacked structure shown in (A). The consistent destructive SHG responses demonstrate the coherent nature of the as-grown WS₂ ribbon arrays. (C) The polarization-dependent SHG patterns collected from different bare ribbons in (A).

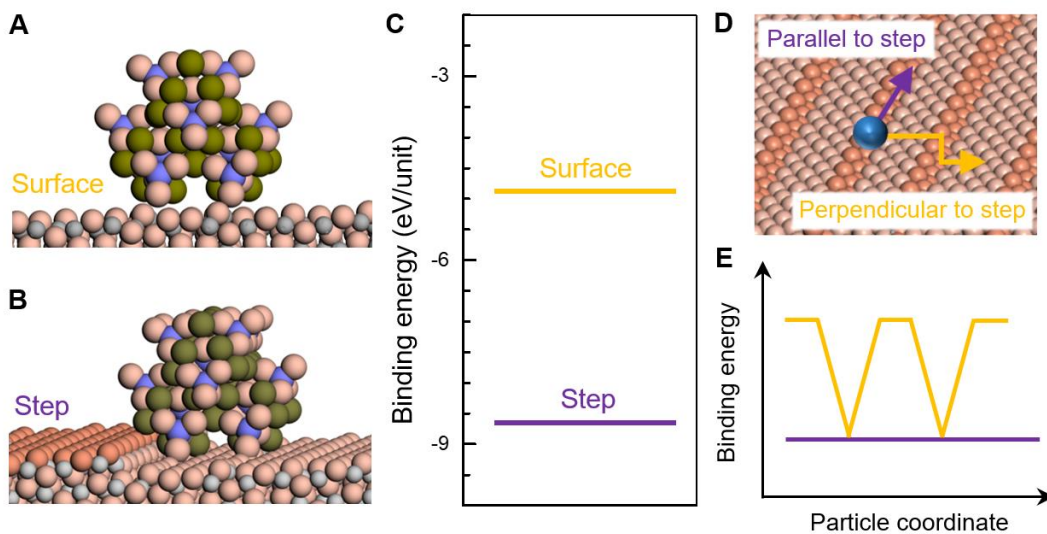


Fig. S7. DFT calculations of Na_2WO_4 particles on sapphire substrates. (A and B) Schematic for the configuration of Na_2WO_4 particle on a flat surface (A) and step edge (B) of sapphire substrate. (C) The calculated binding energies of the two different configurations on sapphire. (D and E) Schematic for the particle movement (D) and energy profiles (E) of parallel (violet curve) and perpendicular (yellow curve) to the step edges, respectively. Any movement of a particle away from a step edge will lead to an increased energy of the whole system.

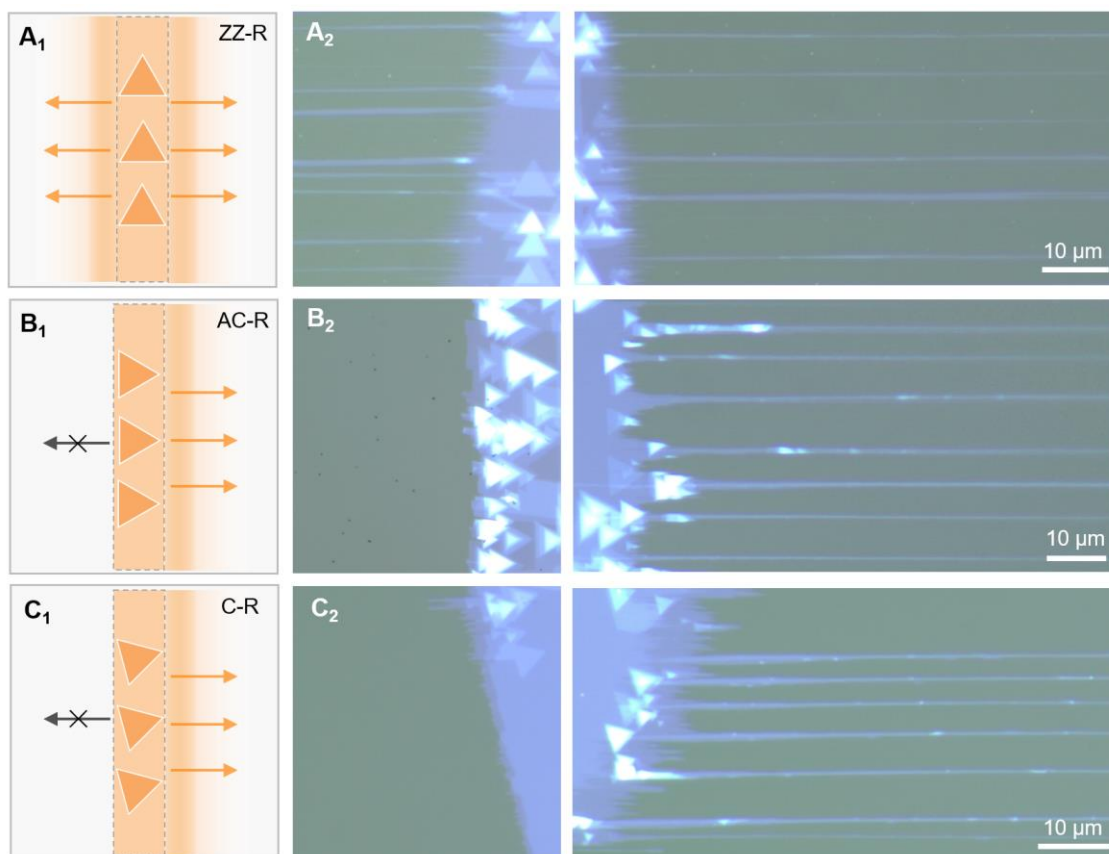


Fig. S8. Optical images of the nucleated WS₂ domains and ribbons. (A) Zigzag ribbons grown from both sides of nucleated WS₂ domains. (B and C) Armchair and chiral ribbons preferred a unidirectional growth on one side.

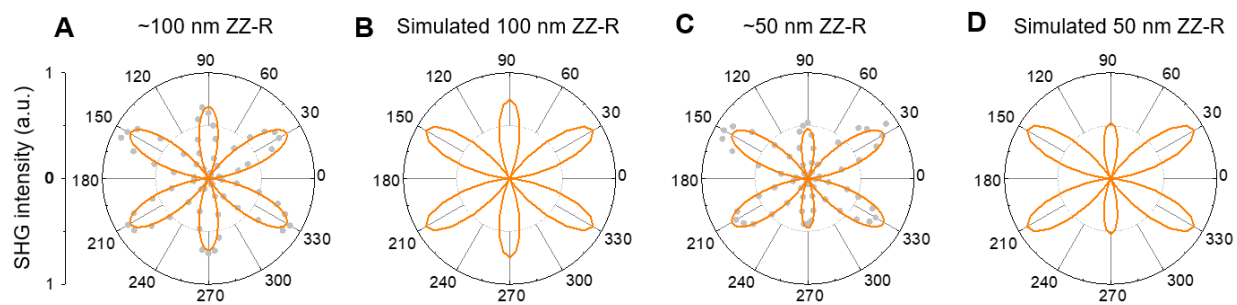


Fig. S9. Distortion of the polarization-dependent SHG patterns in WS₂ ribbons. (A and B) Experimental and simulated SHG patterns of zigzag WS₂ ribbons with width of 100 nm. **(C and D)** Experimental and simulated SHG patterns of zigzag WS₂ ribbons with width of 50 nm.

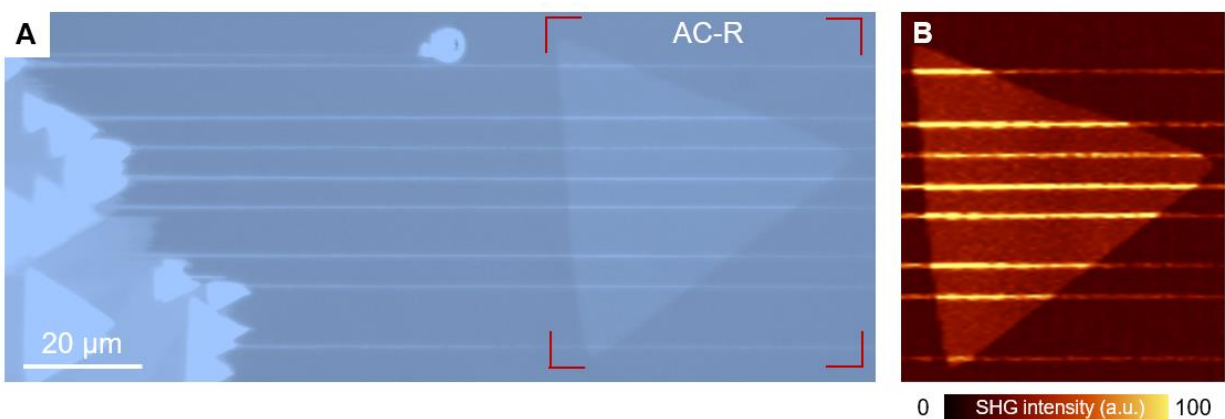


Fig. S10. Coherent characteristic of the armchair ribbon array. (A) Optical image of the armchair ribbons covered with a triangular monolayer WS_2 domain. (B) SHG mapping of the armchair ribbons/ WS_2 stacked structure. The consistent enhancement of SHG signal indicated the coherent polarity direction throughout the armchair ribbon array.

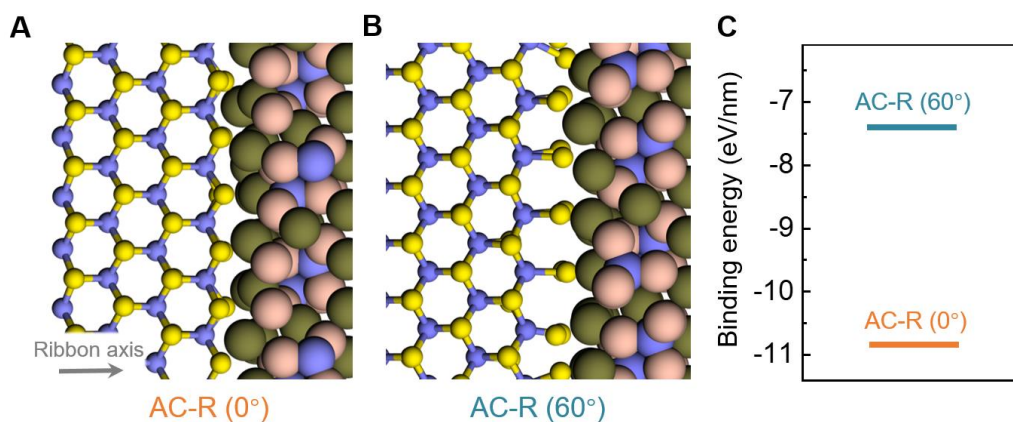


Fig. S11. Calculated interfacial energies between WS_2 ribbons and Na_2WO_4 precursors. (A and B) Schematics of the interface between Na_2WO_4 cluster with AC-R (0°) (A) and twinned AC-R (60°) (B), respectively. The arrow in (A) indicates the axis orientation of WS_2 ribbon. The pink, dark yellow, yellow and violet balls represent the top O atoms, Na atoms, S atoms and W atoms, respectively. (C) Calculated binding energies of the two types of contact interfaces.

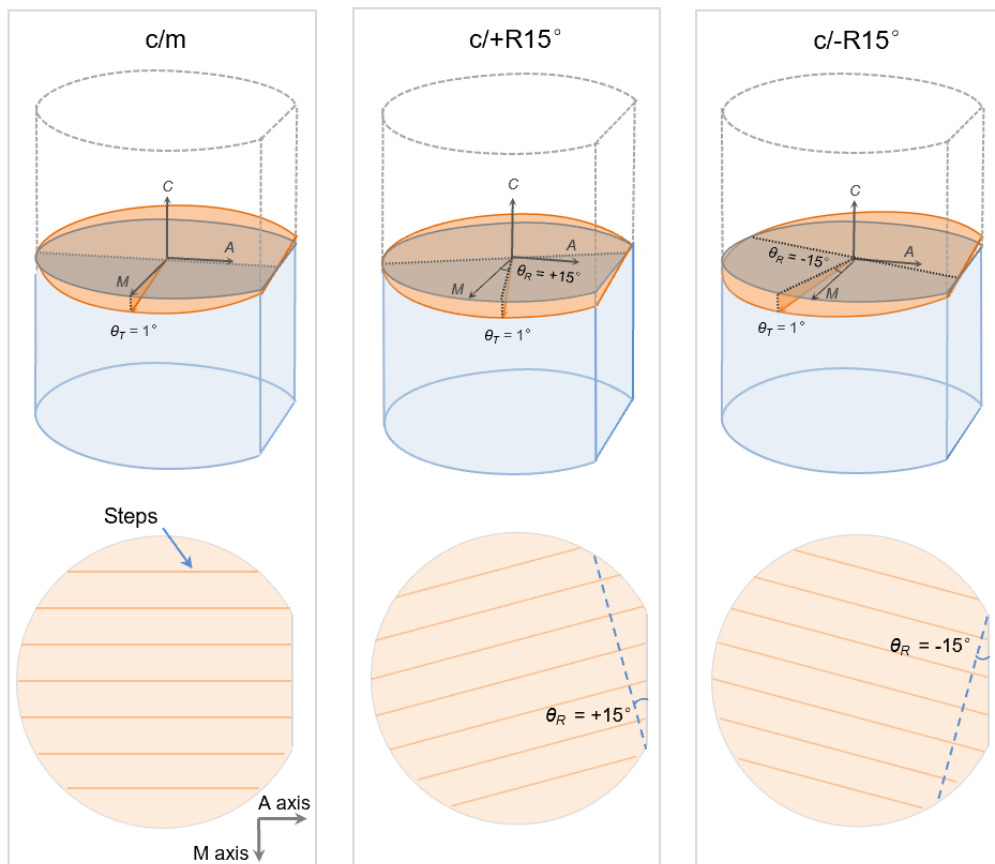


Fig. S12. Step orientation design by miscutting the c-plane sapphire wafers from an ingot.

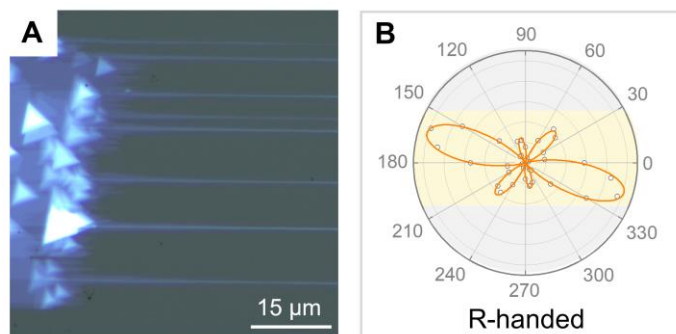


Fig. S13. Characterization of right-handed WS₂ ribbons. (A) Optical image of the as-grown R-handed WS₂ ribbons. (B) Typical polarization-dependent SHG pattern of a R-handed WS₂ ribbon.

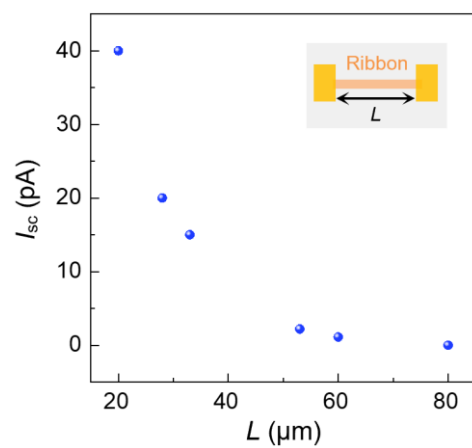


Fig. S14. Short-circuit current (I_{sc}) variation with channel lengths (L) in armchair ribbons.

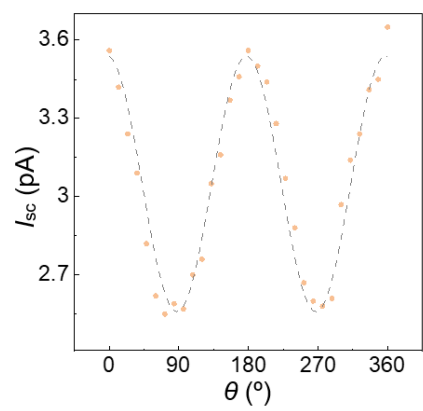


Fig. S15. The polarization-dependent short-circuit current of an armchair ribbon with ~80-nm width.

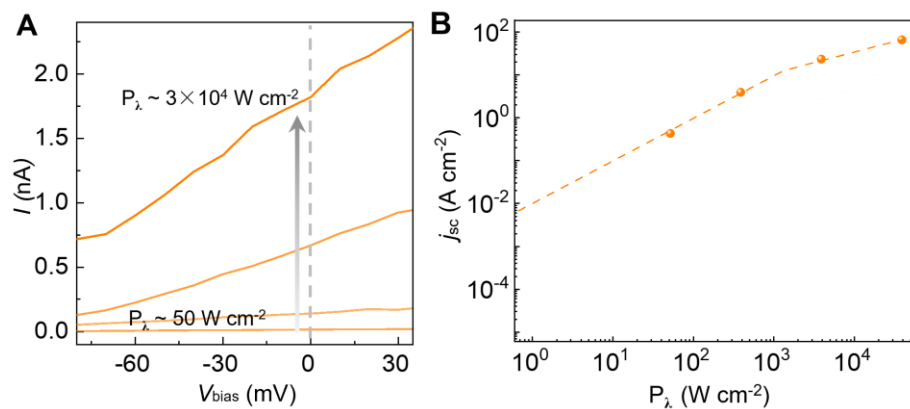


Fig. S16. The enhanced BPVE in thick WS₂ ribbons. (A) Representative I - V characteristics of a 14-nm-thick armchair ribbon under the illumination power density from 50 to $3 \times 10^4 \text{ W cm}^{-2}$. (B) The BPVE short-circuit current density versus incident power density in the 14-nm-thick ribbon.

References and Notes

1. M.-M. Yang, D. J. Kim, M. Alexe, Flexo-photovoltaic effect. *Science* **360**, 904–907 (2018). [doi:10.1126/science.aan3256](https://doi.org/10.1126/science.aan3256) [Medline](#)
2. T. Akamatsu, T. Ideue, L. Zhou, Y. Dong, S. Kitamura, M. Yoshii, D. Yang, M. Onga, Y. Nakagawa, K. Watanabe, T. Taniguchi, J. Laurienzo, J. Huang, Z. Ye, T. Morimoto, H. Yuan, Y. Iwasa, A van der Waals interface that creates in-plane polarization and a spontaneous photovoltaic effect. *Science* **372**, 68–72 (2021). [doi:10.1126/science.aaz9146](https://doi.org/10.1126/science.aaz9146) [Medline](#)
3. J. Jiang, Z. Chen, Y. Hu, Y. Xiang, L. Zhang, Y. Wang, G.-C. Wang, J. Shi, Flexo-photovoltaic effect in MoS₂. *Nat. Nanotechnol.* **16**, 894–901 (2021). [doi:10.1038/s41565-021-00919-y](https://doi.org/10.1038/s41565-021-00919-y) [Medline](#)
4. D. Yang, J. Wu, B. T. Zhou, J. Liang, T. Ideue, T. Siu, K. M. Awan, K. Watanabe, T. Taniguchi, Y. Iwasa, M. Franz, Z. Ye, Spontaneous-polarization-induced photovoltaic effect in rhombohedrally stacked MoS₂. *Nat. Photonics* **16**, 469–474 (2022). [doi:10.1038/s41566-022-01008-9](https://doi.org/10.1038/s41566-022-01008-9)
5. Y. Dong, M.-M. Yang, M. Yoshii, S. Matsuoka, S. Kitamura, T. Hasegawa, N. Ogawa, T. Morimoto, T. Ideue, Y. Iwasa, Giant bulk piezophotovoltaic effect in 3R-MoS₂. *Nat. Nanotechnol.* **18**, 36–41 (2023). [doi:10.1038/s41565-022-01252-8](https://doi.org/10.1038/s41565-022-01252-8) [Medline](#)
6. S. Y. Yang, J. Seidel, S. J. Byrnes, P. Shafer, C.-H. Yang, M. D. Rossell, P. Yu, Y.-H. Chu, J. F. Scott, J. W. Ager 3rd, L. W. Martin, R. Ramesh, Above-bandgap voltages from ferroelectric photovoltaic devices. *Nat. Nanotechnol.* **5**, 143–147 (2010). [doi:10.1038/nnano.2009.451](https://doi.org/10.1038/nnano.2009.451) [Medline](#)
7. J. E. Spanier, V. M. Fridkin, A. M. Rappe, A. R. Akbashev, A. Polemi, Y. Qi, Z. Gu, S. M. Young, C. J. Hawley, D. Imbrenda, G. Xiao, A. L. Bennett-Jackson, C. L. Johnson, Power conversion efficiency exceeding the Shockley–Queisser limit in a ferroelectric insulator. *Nat. Photonics* **10**, 611–616 (2016). [doi:10.1038/nphoton.2016.143](https://doi.org/10.1038/nphoton.2016.143)
8. M. Nakamura, S. Horiuchi, F. Kagawa, N. Ogawa, T. Kurumaji, Y. Tokura, M. Kawasaki, Shift current photovoltaic effect in a ferroelectric charge-transfer complex. *Nat. Commun.* **8**, 281 (2017). [doi:10.1038/s41467-017-00250-y](https://doi.org/10.1038/s41467-017-00250-y) [Medline](#)
9. L. Du, T. Hasan, A. Castellanos-Gomez, G.-B. Liu, Y. Yao, C. N. Lau, Z. Sun, Engineering symmetry breaking in 2D layered materials. *Nat. Rev. Phys.* **3**, 193–206 (2021). [doi:10.1038/s42254-020-00276-0](https://doi.org/10.1038/s42254-020-00276-0)
10. Y. J. Zhang, T. Ideue, M. Onga, F. Qin, R. Suzuki, A. Zak, R. Tenne, J. H. Smet, Y. Iwasa, Enhanced intrinsic photovoltaic effect in tungsten disulfide nanotubes. *Nature* **570**, 349–353 (2019). [doi:10.1038/s41586-019-1303-3](https://doi.org/10.1038/s41586-019-1303-3) [Medline](#)
11. M. M. Yang, M. Alexe, Sunlight harvested by nanotubes. *Nature* **570**, 310–311 (2019). [doi:10.1038/d41586-019-01767-6](https://doi.org/10.1038/d41586-019-01767-6) [Medline](#)
12. S. Li, Y.-C. Lin, W. Zhao, J. Wu, Z. Wang, Z. Hu, Y. Shen, D.-M. Tang, J. Wang, Q. Zhang, H. Zhu, L. Chu, W. Zhao, C. Liu, Z. Sun, T. Taniguchi, M. Osada, W. Chen, Q.-H. Xu, A. T. S. Wee, K. Suenaga, F. Ding, G. Eda, Vapour-liquid-solid growth of monolayer

- MoS₂ nanoribbons. *Nat. Mater.* **17**, 535–542 (2018). [doi:10.1038/s41563-018-0055-z](https://doi.org/10.1038/s41563-018-0055-z) [Medline](#)
13. A. Aljarb, J.-H. Fu, C.-C. Hsu, C.-P. Chuu, Y. Wan, M. Hakami, D. R. Naphade, E. Yengel, C.-J. Lee, S. Brems, T.-A. Chen, M.-Y. Li, S.-H. Bae, W.-T. Hsu, Z. Cao, R. Albaridy, S. Lopatin, W.-H. Chang, T. D. Anthopoulos, J. Kim, L.-J. Li, V. Tung, Ledge-directed epitaxy of continuously self-aligned single-crystalline nanoribbons of transition metal dichalcogenides. *Nat. Mater.* **19**, 1300–1306 (2020). [doi:10.1038/s41563-020-0795-4](https://doi.org/10.1038/s41563-020-0795-4) [Medline](#)
 14. Y. Deng, C. Zhu, Y. Wang, X. Wang, X. Zhao, Y. Wu, B. Tang, R. Duan, K. Zhou, Z. Liu, Lithography-free, high-density MoTe₂ nanoribbon arrays. *Mater. Today* **58**, 8–17 (2022). [doi:10.1016/j.mattod.2022.06.002](https://doi.org/10.1016/j.mattod.2022.06.002)
 15. P. Yang, D. Wang, X. Zhao, W. Quan, Q. Jiang, X. Li, B. Tang, J. Hu, L. Zhu, S. Pan, Y. Shi, Y. Huan, F. Cui, S. Qiao, Q. Chen, Z. Liu, X. Zou, Y. Zhang, Epitaxial growth of inch-scale single-crystal transition metal dichalcogenides through the patching of unidirectionally orientated ribbons. *Nat. Commun.* **13**, 3238 (2022). [doi:10.1038/s41467-022-30900-9](https://doi.org/10.1038/s41467-022-30900-9) [Medline](#)
 16. X. Liu, T. Xu, X. Wu, Z. Zhang, J. Yu, H. Qiu, J.-H. Hong, C.-H. Jin, J.-X. Li, X.-R. Wang, L.-T. Sun, W. Guo, Top-down fabrication of sub-nanometre semiconducting nanoribbons derived from molybdenum disulfide sheets. *Nat. Commun.* **4**, 1776 (2013). [doi:10.1038/ncomms2803](https://doi.org/10.1038/ncomms2803) [Medline](#)
 17. Z. Liu, K. Suenaga, Z. Wang, Z. Shi, E. Okunishi, S. Iijima, Identification of active atomic defects in a monolayered tungsten disulphide nanoribbon. *Nat. Commun.* **2**, 213 (2011). [doi:10.1038/ncomms1224](https://doi.org/10.1038/ncomms1224) [Medline](#)
 18. Y. Chen, P. Cui, X. Ren, C. Zhang, C. Jin, Z. Zhang, C.-K. Shih, Fabrication of MoSe₂ nanoribbons via an unusual morphological phase transition. *Nat. Commun.* **8**, 15135 (2017). [doi:10.1038/ncomms15135](https://doi.org/10.1038/ncomms15135) [Medline](#)
 19. F. Cheng, H. Xu, W. Xu, P. Zhou, J. Martin, K. P. Loh, Controlled growth of 1D MoSe₂ nanoribbons with spatially modulated edge states. *Nano Lett.* **17**, 1116–1120 (2017). [doi:10.1021/acs.nanolett.6b04715](https://doi.org/10.1021/acs.nanolett.6b04715) [Medline](#)
 20. T. Chowdhury, J. Kim, E. C. Sadler, C. Li, S. W. Lee, K. Jo, W. Xu, D. H. Gracias, N. V. Drichko, D. Jariwala, T. H. Brintlinger, T. Mueller, H.-G. Park, T. J. Kempa, Substrate-directed synthesis of MoS₂ nanocrystals with tunable dimensionality and optical properties. *Nat. Nanotechnol.* **15**, 29–34 (2020). [doi:10.1038/s41565-019-0571-2](https://doi.org/10.1038/s41565-019-0571-2) [Medline](#)
 21. R. Xiang, T. Inoue, Y. Zheng, A. Kumamoto, Y. Qian, Y. Sato, M. Liu, D. Tang, D. Gokhale, J. Guo, K. Hisama, S. Yotsumoto, T. Ogamoto, H. Arai, Y. Kobayashi, H. Zhang, B. Hou, A. Anisimov, M. Maruyama, Y. Miyata, S. Okada, S. Chiashi, Y. Li, J. Kong, E. I. Kauppinen, Y. Ikuhara, K. Suenaga, S. Maruyama, One-dimensional van der Waals heterostructures. *Science* **367**, 537–542 (2020). [doi:10.1126/science.aaz2570](https://doi.org/10.1126/science.aaz2570) [Medline](#)
 22. X. Li, B. Li, J. Lei, K. V. Bets, X. Sang, E. Okogbue, Y. Liu, R. R. Unocic, B. I. Yakobson, J. Hone, A. R. Harutyunyan, Nickel particle-enabled width-controlled growth of bilayer

- molybdenum disulfide nanoribbons. *Sci Adv* **7**, eabk1892 (2021). [doi:10.1126/sciadv.abk1892](https://doi.org/10.1126/sciadv.abk1892) [Medline](#)
23. Q. An, W. Xiong, F. Hu, Y. Yu, P. Lv, S. Hu, X. Gan, X. He, J. Zhao, S. Yuan, Direct growth of single-chiral-angle tungsten disulfide nanotubes using gold nanoparticle catalysts. *Nat. Mater.* **23**, 347–355 (2024). [doi:10.1038/s41563-023-01590-5](https://doi.org/10.1038/s41563-023-01590-5) [Medline](#)
24. J. R. Sanchez-Valencia, T. Dienel, O. Gröning, I. Shorubalko, A. Mueller, M. Jansen, K. Amsharov, P. Ruffieux, R. Fasel, Controlled synthesis of single-chirality carbon nanotubes. *Nature* **512**, 61–64 (2014). [doi:10.1038/nature13607](https://doi.org/10.1038/nature13607) [Medline](#)
25. R. M. Jacobberger, B. Kiraly, M. Fortin-Deschenes, P. L. Levesque, K. M. McElhinny, G. J. Brady, R. Rojas Delgado, S. Singha Roy, A. Mannix, M. G. Lagally, P. G. Evans, P. Desjardins, R. Martel, M. C. Hersam, N. P. Guisinger, M. S. Arnold, Direct oriented growth of armchair graphene nanoribbons on germanium. *Nat. Commun.* **6**, 8006 (2015). [doi:10.1038/ncomms9006](https://doi.org/10.1038/ncomms9006) [Medline](#)
26. S. Zhang, L. Kang, X. Wang, L. Tong, L. Yang, Z. Wang, K. Qi, S. Deng, Q. Li, X. Bai, F. Ding, J. Zhang, Arrays of horizontal carbon nanotubes of controlled chirality grown using designed catalysts. *Nature* **543**, 234–238 (2017). [doi:10.1038/nature21051](https://doi.org/10.1038/nature21051) [Medline](#)
27. H. S. Wang, L. Chen, K. Elibol, L. He, H. Wang, C. Chen, C. Jiang, C. Li, T. Wu, C. X. Cong, T. J. Pennycook, G. Argentero, D. Zhang, K. Watanabe, T. Taniguchi, W. Wei, Q. Yuan, J. C. Meyer, X. Xie, Towards chirality control of graphene nanoribbons embedded in hexagonal boron nitride. *Nat. Mater.* **20**, 202–207 (2021). [doi:10.1038/s41563-020-00806-2](https://doi.org/10.1038/s41563-020-00806-2) [Medline](#)
28. J. Cai, P. Ruffieux, R. Jaafar, M. Bieri, T. Braun, S. Blankenburg, M. Muoth, A. P. Seitsonen, M. Saleh, X. Feng, K. Müllen, R. Fasel, Atomically precise bottom-up fabrication of graphene nanoribbons. *Nature* **466**, 470–473 (2010). [doi:10.1038/nature09211](https://doi.org/10.1038/nature09211) [Medline](#)
29. Y. Zuo, C. Liu, L. Ding, R. Qiao, J. Tian, C. Liu, Q. Wang, G. Xue, Y. You, Q. Guo, J. Wang, Y. Fu, K. Liu, X. Zhou, H. Hong, M. Wu, X. Lu, R. Yang, G. Zhang, D. Yu, E. Wang, X. Bai, F. Ding, K. Liu, Robust growth of two-dimensional metal dichalcogenides and their alloys by active chalcogen monomer supply. *Nat. Commun.* **13**, 1007 (2022). [doi:10.1038/s41467-022-28628-7](https://doi.org/10.1038/s41467-022-28628-7) [Medline](#)
30. P. Deb, M. C. Cao, Y. Han, M. E. Holtz, S. Xie, J. Park, R. Hovden, D. A. Muller, Imaging polarity in two dimensional materials by breaking Friedel’s law. *Ultramicroscopy* **215**, 113019 (2020). [doi:10.1016/j.ultramic.2020.113019](https://doi.org/10.1016/j.ultramic.2020.113019) [Medline](#)
31. S. Han, X. Liu, C. Zhou, Template-free directional growth of single-walled carbon nanotubes on *a*- and *r*-plane sapphire. *J. Am. Chem. Soc.* **127**, 5294–5295 (2005). [doi:10.1021/ja042544x](https://doi.org/10.1021/ja042544x) [Medline](#)
32. D. Tsivion, M. Schvartzman, R. Popovitz-Biro, P. von Huth, E. Joselevich, Guided growth of millimeter-long horizontal nanowires with controlled orientations. *Science* **333**, 1003–1007 (2011). [doi:10.1126/science.1208455](https://doi.org/10.1126/science.1208455) [Medline](#)
33. Z. Ma, S. Wang, Q. Deng, Z. Hou, X. Zhou, X. Li, F. Cui, H. Si, T. Zhai, H. Xu, Epitaxial growth of rectangle shape MoS₂ with highly aligned orientation on twofold symmetry *a*-plane sapphire. *Small* **16**, e2000596 (2020). [doi:10.1002/sml.202000596](https://doi.org/10.1002/sml.202000596) [Medline](#)

34. J. Wang, X. Xu, T. Cheng, L. Gu, R. Qiao, Z. Liang, D. Ding, H. Hong, P. Zheng, Z. Zhang, Z. Zhang, S. Zhang, G. Cui, C. Chang, C. Huang, J. Qi, J. Liang, C. Liu, Y. Zuo, G. Xue, X. Fang, J. Tian, M. Wu, Y. Guo, Z. Yao, Q. Jiao, L. Liu, P. Gao, Q. Li, R. Yang, G. Zhang, Z. Tang, D. Yu, E. Wang, J. Lu, Y. Zhao, S. Wu, F. Ding, K. Liu, Dual-coupling-guided epitaxial growth of wafer-scale single-crystal WS₂ monolayer on vicinal a-plane sapphire. *Nat. Nanotechnol.* **17**, 33–38 (2022). [doi:10.1038/s41565-021-01004-0](https://doi.org/10.1038/s41565-021-01004-0) [Medline](#)
35. P. Zheng, W. Wei, Z. Liang, B. Qin, J. Tian, J. Wang, R. Qiao, Y. Ren, J. Chen, C. Huang, X. Zhou, G. Zhang, Z. Tang, D. Yu, F. Ding, K. Liu, X. Xu, Universal epitaxy of non-centrosymmetric two-dimensional single-crystal metal dichalcogenides. *Nat. Commun.* **14**, 592 (2023). [doi:10.1038/s41467-023-36286-6](https://doi.org/10.1038/s41467-023-36286-6) [Medline](#)
36. T. Li, W. Guo, L. Ma, W. Li, Z. Yu, Z. Han, S. Gao, L. Liu, D. Fan, Z. Wang, Y. Yang, W. Lin, Z. Luo, X. Chen, N. Dai, X. Tu, D. Pan, Y. Yao, P. Wang, Y. Nie, J. Wang, Y. Shi, X. Wang, Epitaxial growth of wafer-scale molybdenum disulfide semiconductor single crystals on sapphire. *Nat. Nanotechnol.* **16**, 1201–1207 (2021). [doi:10.1038/s41565-021-00963-8](https://doi.org/10.1038/s41565-021-00963-8) [Medline](#)
37. J.-H. Fu, J. Min, C.-K. Chang, C.-C. Tseng, Q. Wang, H. Sugisaki, C. Li, Y.-M. Chang, I. Alnami, W.-R. Syong, C. Lin, F. Fang, L. Zhao, T.-H. Lo, C.-S. Lai, W.-S. Chiu, Z.-S. Jian, W.-H. Chang, Y.-J. Lu, K. Shih, L.-J. Li, Y. Wan, Y. Shi, V. Tung, Oriented lateral growth of two-dimensional materials on *c*-plane sapphire. *Nat. Nanotechnol.* **18**, 1289–1294 (2023). [doi:10.1038/s41565-023-01445-9](https://doi.org/10.1038/s41565-023-01445-9) [Medline](#)
38. Z. Liang, X. Zhou, L. Zhang, X.-L. Yu, Y. Lv, X. Song, Y. Zhou, H. Wang, S. Wang, T. Wang, P. P. Shum, Q. He, Y. Liu, C. Zhu, L. Wang, X. Chen, Strong bulk photovoltaic effect in engineered edge-embedded van der Waals structures. *Nat. Commun.* **14**, 4230 (2023). [doi:10.1038/s41467-023-39995-0](https://doi.org/10.1038/s41467-023-39995-0) [Medline](#)